International Journal of Robotics and Automation, Vol. 36, 2021

Special Issue: Automatic Detection and Assessment of Bridge Structures

LINE SHAPE MONITORING OF LONG-SPAN CONCRETE-FILLED STEEL TUBE ARCHES BASED ON THREE-DIMENSIONAL LASER SCANNING

Mingshu Sun,* Anqi Xu,** and Jian Liu***

Abstract

Conventional line shape monitoring methods applied to bridges collect observation data only for multiple independent points, which makes obtaining comprehensive and accurate deformation information for the entire bridge very difficult. This has been addressed by the application of three-dimensional (3D) laser scanning technology, which has expanded the range of line shape monitoring, increased the measurement speed, and improved observation accuracy. However, the monitoring precision of 3D laser scanning technology has not been rigorously demonstrated for long-span bridges subject to large-scale temperature fluctuations. This study addresses this issue by applying 3D laser scanning technology for monitoring the line shape of a concrete-filled steel tube arch bridge with a main span of 300 m under conditions where the temperatures of the main arch components vary due to irregular heating. The results of 3D laser scanning are verified by comparison with the results of simulations using Midas Civil. The measurement results obtained by 3D laser scanning are found to be consistent with the simulation results, and the measured values exhibit a higher precision, which verifies the reliability of 3D laser scanning technology when applied to long-span bridge line shape monitoring.

Key Words

3D laser scanning technology, bridge line shape monitoring, finite element analysis, temperature

1. Introduction

Evaluating changes in the line shape of bridges is an essential aspect of bridge construction monitoring; however, conventional line shape monitoring methods collect observation data only for multiple independent points, which makes obtaining comprehensive and accurate deformation information for the entire bridge very difficult [1], [2]. This has been addressed by the application of three-dimensional (3D) laser scanning technology, which can quickly obtain the 3D coordinates of entire bridge structures with improved observation accuracy. As a result, this technology has been widely applied in a wide variety of fields, such as civil engineering, industrial measurement, and medicine [3], [4].

The benefits of applying 3D laser scanning technology in bridge engineering have been extensively demonstrated. For example, Ma *et al.* [5], [6] applied this technology for monitoring the construction of large-span steel structures, and the accuracy and efficiency of the technology were demonstrated by comparing the obtained deformation results with those of feature points. Yoon *et al.* [7] applied the technique to obtain position data for prefabricated slabs and beams. These position data were employed to estimate the size of error using density-based clustering of applications with noise (DBSCAN) and mixed pixel filtering algorithms, and the optimal layout of the slabs relative to the beams was obtained by solving a nonlinear minimization problem. Riveiro *et al.* [8] employed a 3D laser scanning system to obtain the true 3D shape of a stone arch bridge listed as a World Heritage site, and these data were combined with numerical simulation analysis to estimate its critical load. Soni *et al.* [9], [10] applied the 3D laser scanning technology to obtain the exact geometric dimensions of ancient arch bridges with no design parameters. Then, statistical nonparametric methods were employed to process the point data and thereby analyse the deformation of the arches.

While the above-discussed research has demonstrated the feasibility of 3D laser scanning technology for the line shape monitoring of bridges, this technology has been only rarely applied to long-span bridges, and the reliability of this technology has not yet been rigorously demonstrated

* Southwest Transportation Construction Group Co., Ltd., Sichuan, China; e-mail: 1194874602@qq.com
** CCCC Second Harbour Engineering Co., Ltd., National Enterprise Technology Center, Wuhan, China; e-mail: xuanqi94@q163.com
*** CMCU Engineering Co., Ltd., Chongqing, China, e-mail: 1343174313@qq.com
Corresponding author: Mingshu Sun
Recommended by Dr. Jingzhou Xin
(DOI: 10.2316/J.2021.206-0541)

for bridges subject to large-scale temperature fluctuations. This study addresses these issues by applying the 3D laser scanning technology for monitoring the line shape of the upper variable-section truss arch of a concrete-filled steel tube (CFST) arch bridge with a main span of 300 m under conditions where the temperatures of the main arch components vary due to irregular heating. The accuracy of 3D laser scanning technology when applied to measurements of the main arch of long-span arch bridges is studied from the aspects of data acquisition and data processing. For comparison, the bridge is modelled using the finite element analysis software Midas Civil to obtain the deformations of the main arch under irregular temperature distributions, and the good agreement between the measurement results and the simulation results demonstrates the feasibility of applying 3D laser scanning technology for analysing the effect of temperature on the main arch structure.

2. Working Principles of 3D Scanning Technology

2.1 Scanning Principle of Laser System

The process of scanning a single measurement point P using a 3D laser scanner positioned at the origin O of a Cartesian coordinate system is illustrated in Fig. 1. Here, the X and Y axes are on the horizontal plane of the local coordinate system, and the Z-axis is the vertical direction. The scanning process obtains the slant distance S, horizontal angle φ and vertical angle θ from each scanning point and transmits this data to the laser emission centre of the scanner simultaneously. The 3D coordinates of the target point P can then be calculated using S, φ and θ as follows [11]:

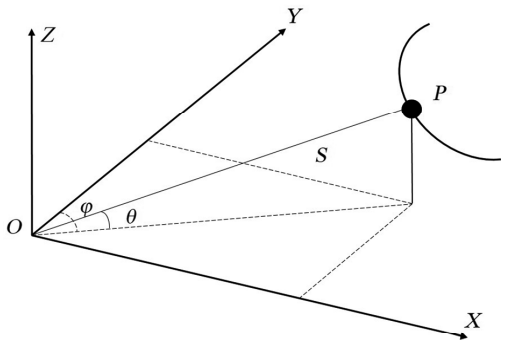

Figure 1. Schematic illustrating the 3D laser scanning of a single measurement point P.

$$\begin{cases} X = S\cos\theta\sin\varphi \\ Y = S\cos\theta\cos\varphi \\ Z = S\cos\theta \end{cases} \tag{1}$$

The present work employs the FARO Focus3D X 330 3D laser scanner and the Leica Nova MS60 Multistation. The main technical parameters of these systems are listed in Table 1.

2.2 Multi-view Point Cloud Processing

Point information is collected from different fields of view in the 3D laser scanning process and is therefore generally referred to as a multi-view point cloud. Moreover, the coordinate systems defining the point cloud data obtained from different azimuth angles are also different. Generally, the point cloud data collected from different azimuth angles are imported into a unified coordinate system to describe the complete surface information of an object. This processing of multi-view point cloud data produces what is denoted as a mosaic configuration.

The transformation of point cloud data collected from different azimuth angles into a unified coordinate system generally involves translation, rotation, and scaling operations [12], which are defined as follows:

(1) Point cloud translation is defined as follows:

$$[x_i\ y_i\ z_i\ 1] = [x\ y\ z\ 1]\begin{bmatrix} 1 & 0 & 0 & 0 \\ 0 & 1 & 0 & 0 \\ 0 & 0 & 1 & 0 \\ t_x & t_y & t_z & 1 \end{bmatrix}. \tag{2}$$

Here, t_x, t_y, and t_z represent the respective distances by which the coordinates of a point are translated along the x, y, and z axes, which can be expressed as follows:

$$\begin{cases} x_i = x + t_x \\ y_i = y + t_y \\ z_i = y + t_z \end{cases} \tag{3}$$

(2) Point cloud rotation through an arbitrary angle θ represents a more complex transformation because the

Table 1
Main Technical Parameters of the 3D Laser Scanning Instruments Employed in the Present Study

Instrument	Measurement Distance (m)	Scan Speed (dots/second)	Horizontal Vertical Measurement Range (°)	Distance Measurement Error (mm)
FARO Focus3D X 330	0.6–330	976,000 (maximum mining point rate)	360 × 300	±2 at 10 m and 25 m
Leica MS60	No prism 1.5–2000	500,000 (maximum picking rate)	360 × 310	±2 at 25 m ±3 at 50 m

rotation axis and the rotation angle are generally not fixed when the point cloud data is rotated in three dimensions. Here, point cloud rotation, when taking the x-axis as the axis of rotation, is defined as follows:

$$\begin{bmatrix} x_i \\ y_i \\ z_i \\ 1 \end{bmatrix} = \begin{bmatrix} 1 & 0 & 0 & 0 \\ 0 & \cos\theta & -\sin\theta & 0 \\ 0 & \sin\theta & \cos\theta & 0 \\ 0 & 0 & 0 & 1 \end{bmatrix} \begin{bmatrix} x \\ y \\ z \\ 1 \end{bmatrix} \tag{4}$$

Taking the y-axis as the axis of rotation yields the following:

$$\begin{bmatrix} x_i \\ y_i \\ z_i \\ 1 \end{bmatrix} = \begin{bmatrix} \cos\theta & 0 & \sin\theta & 0 \\ 0 & 1 & 0 & 0 \\ -\sin\theta & 0 & \cos\theta & 0 \\ 0 & 0 & 0 & 1 \end{bmatrix} \begin{bmatrix} x \\ y \\ z \\ 1 \end{bmatrix} \tag{5}$$

Finally, taking the z-axis as the axis of rotation axis yields the following:

$$\begin{bmatrix} x_i \\ y_i \\ z_i \\ 1 \end{bmatrix} = \begin{bmatrix} \cos\theta & -\sin\theta & 0 & 0 \\ \sin\theta & \cos\theta & 0 & 0 \\ 0 & 0 & 1 & 0 \\ 0 & 0 & 0 & 1 \end{bmatrix} \begin{bmatrix} x \\ y \\ z \\ 1 \end{bmatrix} \tag{6}$$

(3) Point cloud scaling involves decreasing or increasing the scale of the point cloud to observe more or less of its local details. Point cloud scaling is defined as follows:

$$[x_i\ y_i\ z_i\ 1] = [x\ y\ z\ 1] \begin{bmatrix} l_x & 0 & 0 & 0 \\ 0 & l_y & 0 & 0 \\ 0 & 0 & l_z & 0 \\ 0 & 0 & 0 & 1 \end{bmatrix} \tag{7}$$

Here, l_x, l_y, and l_z represent the scaling factors employed in the x, y, and z directions, respectively. The original geometric shape of the object is typically conserved by employing the same scaling method.

2.3 3D Reconstruction Accuracy of Point Cloud Data

The 3D reconstruction accuracy of point cloud data was initially verified by a standard comparison process involving the standard deviation in Geomagic Control X software with the calculated average error in the fitted residual, which is conducted using the plane fitting program [13]. To this end, we define the plane equation as follows:

$$p(x, y, z) = ax + by + cz + d = 0, \tag{8}$$

where a, b, c, and d are adjustable parameters. The measured point cloud data composed of n scanned points are defined as (x_i, y_i, z_i) $(i = 1, 2, 3, \ldots, n)$, and the values of a, b, c, and d in (8) that provide the optimum plane representing the collection of measured point cloud data are obtained by least squares fitting as follows:

$$\text{minimize} \sum\nolimits_{i=0}^{n} \left[p(x, y, z) - p(x_i, y_i, z_i)\right]^2 = \min \tag{9}$$

The error in the fitted plane is evaluated by the point distance method. First, we calculate the distance from each laser scanned point to the optimum plane as follows:

$$D = \frac{|ax + by + cz + d|}{\sqrt{a^2 + b^2 + c^2}}. \tag{10}$$

Then, the values of D_i are sorted to find the maximum and minimum values, and an overall evaluation of the error for all points is obtained as follows:

$$\delta = \sqrt{\frac{\sum_{i=1}^{n} D_i^2}{n}}. \tag{11}$$

The 3D reconstruction accuracy of point cloud data is then determined by comparing the coefficient of the equation with the standard deviation obtained by the Geomagic Control X software and comparing the coefficient of the equation calculated by the least squares plane fitting with the overall error δ.

3. Engineering Example

3.1 Project Overview

The bridge serving as the engineering example in the present work is illustrated in Fig. 2 and is a typical super-large bridge built in the deep-cut canyon area of western China. The main bridge component is an upper CFST variable-section truss arch with a net span of 300 m. The main arch has a net height of 54.545 m, a span ratio of 1/5.5, and an arch axis coefficient $m = 1.543$. The bridge deck has a width of 33.5 m, and the bridge deck beams are 20 m first supported and continuous structural T-beam.

3.2 Line Shape Acquisition of Main Arch

3.2.1 Control Point Scanning of Main Arch

Two control points were selected on both the left bank and the right bank of the bridge based on the characteristics of the bridge area. The coordinates of the control points were measured in the geodetic coordinate system using the MS60 Multistation according to the known point coordinates given by the design, and the precision and control points were controlled. The geodetic coordinates of the control points are listed in Table 2, where K1 and K2 are the control points on the right bank, and K3 and K4 are the control points on the left bank.

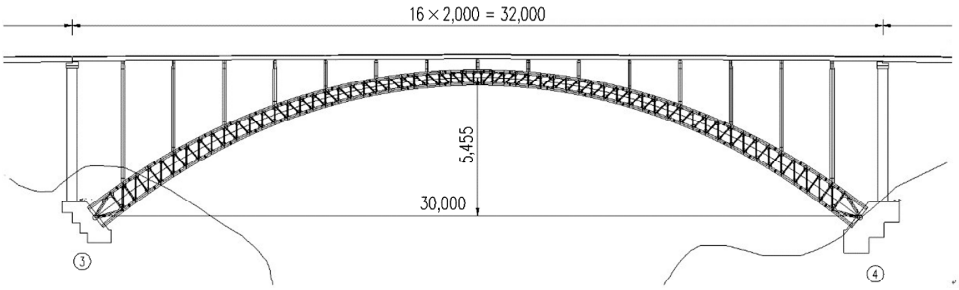

Figure 2. Elevation view of the long-span CFST bridge.

Table 2
3D Coordinates of Control Points

Control Point	X Coordinate (m)	Y Coordinate (m)	Z Coordinate (m)
K1	2,983,957.788	499,735.835	1,090.078
K2	2,983,844.580	499,716.303	1,061.910
K3	2,984,025.716	499,952.939	1,062.913
K4	2,984,246.442	499,895.509	1,105.808

Due to terrain constraints, the entire bridge cannot be scanned in three dimensions at one time. The MS60 Multistation was mainly responsible for conducting the coordinate measurements of the transfer station in preparation for the processing of the post data mosaics. The MS60 Multistation was set at K3, and its 3D laser scanner was employed to scan the corresponding points D1 and D2 on the right bank and point D3 on the left bank with K1 and K2 as the backsight points. Similarly, the whole station scanner conducted coordinate scans of the entire bridge separately.

The scanning process was repeated from 7:00 to 14:00 during the day to evaluate the bridge coordinates under different temperature conditions. For this purpose, the 3D scanner was set at the fixed point D1 on the right bank, and the fixed area of the main arch was scanned every hour. Similarly, the scanner was set at the fixed point K3 (*i.e.*, the sunny side of the bridge) and the fixed point K4 (*i.e.*, the shaded side of the bridge) on the left bank, with K1 and K2 being the backsight points, and the outermost arch rib of the main arch on the sunny and shaded side faces was scanned every hour.

3.2.2 Mosaics of Measured Point Cloud Data

The on-site scanning data were imported into the Geomagic point cloud processing and FARO Scene software for noise reduction and splicing. The MS60 Multistation point cloud data image, FARO Focus3D X 330 overall point cloud data image, and FARO Focus3D X 330 local point cloud data image are presented in Figs. 3(a), (b), and (c), respectively.

It can be seen from Fig. 3 that data cannot be acquired for all points of the entire bridge from only a single perspective due to limitations associated with the conditions in the field. Individual sections of the bridge can be separately scanned later to obtain higher precision data. In addition, it can be packaged by scanning the point cloud, and the shape of the bridge in three dimensions can be displayed while under construction, which plays a vital role in the analysis of the construction state.

3.2.3 3D Reconstruction Accuracy of Main Arch

The reconstruction accuracy of 3D laser scanning data was evaluated using the MS60 Multistation point cloud data image shown in Fig. 3(a) as an example, and the 3D reconstruction results obtained for the main arch segment are presented in Fig. 4. The number of points obtained for each mosaic is different due to the different scanning distances involved, and the reconstructed image includes missing sections. The plane coefficients a, b, and c obtained by least squares fitting according to (9) and from Geomagic Control X software, along with the average fitting errors, which were the standard deviation (Geomagic Control X software) and the value of δ obtained according to (11) (least squares fitting), are presented in Table 3. As can be seen from the table, the coefficients obtained by least squares fitting are consistent with those obtained by the software, and the value of δ is consistent as well with the standard deviation obtained from the software.

The results presented demonstrate that the bridge arch can be reconstructed in three dimensions from the acquired point cloud data. However, relevant error analysis must be conducted to determine whether the shape of the curved surface meets the accuracy requirements based on a comparison of the reconstructed 3D surface with the actual 3D surface. The accuracy requirements are listed in Table 4, where the maximum and minimum thresholds represent the valid range, and the maximum and minimum nominal values represent the usual range. Geomagic Control

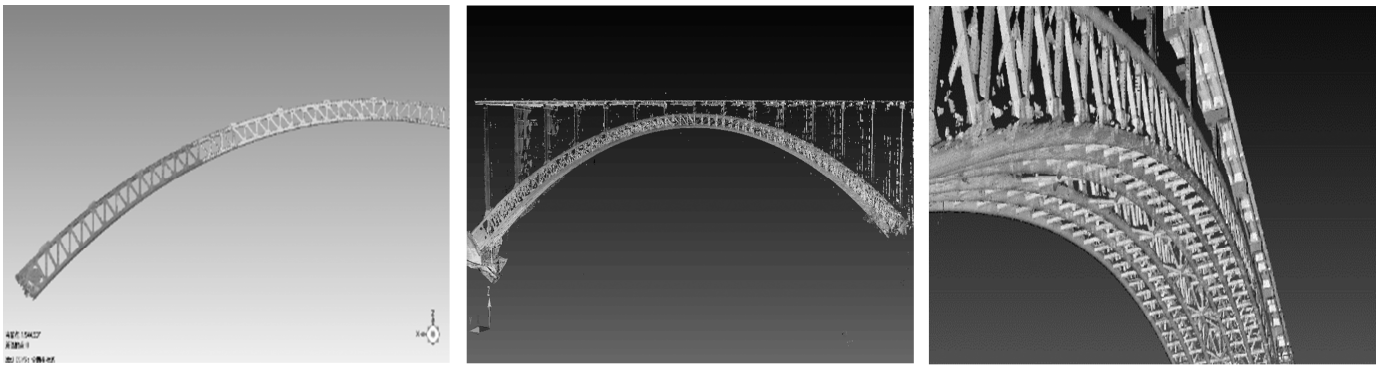

(a) (b) (c)

Figure 3. 3D point cloud displays: (a) Leica Nova MS60 Multistation point cloud data image; (b) FARO Focus3D X 330 overall point cloud data image; and (c) FARO Focus3D X 330 local point cloud data image.

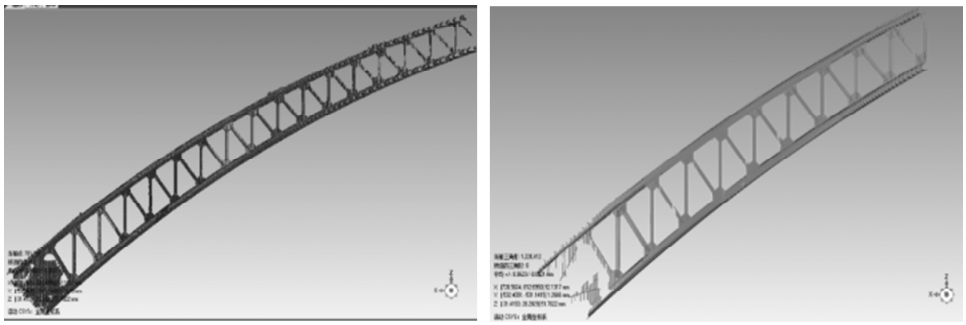

(a) (b)

Figure 4. Leica Nova MS60 Multistation point cloud data reconstruction: (a) point cloud data and (b) after surface fitting.

Table 3
Coefficients and Average Fitting Error Values Obtained During Plane Fitting

Fitting Method	a	b	C	Average Fitting Error (mm)
Least squares plane fitting calculation	0.788	−0.512	−0.005	0.3034
Geomagic Control X software	0.780	−0.516	−0.004	0.3029

Table 4
3D Reconstruction Accuracy (*i.e.*, Deviation) Requirements

Tolerance	Maximum Threshold	Minimum Threshold	Minimum Nominal Value	Maximum Nominal Value
3D deviation (mm)	0.4994	−0.4994	0.0250	−0.0250

X software can apply 3D deviation analysis and model doctors to determine the deviations between the surface of the 3D solid model of the point cloud reconstruction and the actual surface. In addition, the distribution of the deviations reflects the accuracy of the 3D point cloud scanning process, and the number of points lying outside a given deviation range is presented in Table 5, which is automatically generated by the software.

It can be seen from Table 5 that 98% of the points in the reconstructed surface remain within the deviation range of −0.025 to 0.025 mm, and the point cloud reconstruction accuracy meets the requirements. This demonstrates that Geomagic Control X software can be applied for conducting an error analysis of the reconstruction model of the CFST arch bridge obtained from 3D laser scanning. The average fitting error of the surface reconstruction was 0.017 mm, which satisfies the requirements in actual use. This demonstrates that the 3D scanning point cloud data can be used for reverse modelling of the bridge in engineering applications. In addition, we note that model reconstruction was not possible for a few segments of the point cloud data owing to the excessive point cloud error. This

Table 5
Point Cloud Deviation Distributions

≥ Minimum (mm)	<Maximum (mm)	Number of Points	Percent of Total Points (%)
−0.4994	−0.1831	184	0.0704
−0.1831	−0.1041	125	0.0479
−0.1041	−0.0250	1,021	0.3910
−0.0250	0.0250	256,097	98.0696
0.0250	0.1041	2,956	1.1320
0.1041	0.1831	551	0.2110
0.1831	0.2622	203	0.0777
Exceeding the maximum threshold		0	0
Exceeding the minimum threshold		1	0.0004

is primarily due to the limitation of distance during scanning. Reducing the error in the scanning data requires the number of scanning sites and point clouds to be increased as much as possible, which will greatly reduce the level of noise in the point cloud data. It should also be noted that a reconstructed surface that fails to meet the accuracy requirements can be corrected by many strategies, such as adjusting the maximum number of triangles employed in the fitting process, modifying the point spacing, and applying noise reduction, and the surface refitted until the requirements are met.

3.2.4 Two-dimensional Analysis of Main Arch Line Shape

The feasibility of applying 3D laser scanning for conducting line-type analysis of long-span CFST arch bridges is illustrated by comparing the two-dimensional (2D) line shape obtained from 3D laser scanning data with that obtained from the data collected using a Leica TCRA 1201+ total station, where the global coordinate system adopts a geodetic coordinate system. The accuracy of the line shape obtained by 3D scanning was objectively evaluated by comparing the coordinates of specific control points of the main arch segment ranging from the arch foot (point 1) to the vault (point 12) obtained using the two instruments. During point cloud data processing, a Gauss filter function is typically used for data filtering to eliminate noise, reduce data volume by manually eliminating redundant data, and conduct resampling of the point cloud data. Then, the control points and the repetitively scanned reflection target points are used to perform data coordinate correction and point cloud splicing between different stations. The coordinate measurement results collected by 3D laser scanning and the Leica TCRA 1201+ total station are listed in Table 6.

It can be seen from the table that the differences ΔL between the two control point measurements are all less than 1 cm. Accordingly, the accuracy of the 2D line-type data obtained by the 3D laser scanning process is approximately the same as that obtained by the Leica total station. This issue is clarified by plotting the values of ΔL obtained in the X, Y, and Z directions in Fig. 5 for each control point. It can be seen from the figure that the error gradually increases along the arch foot to the arch vault. The main reason is that the large span and location of the bridge in a canyon area necessitates the scanning site to be located on one side of the canyon. As such, the scanning distance gradually increases from the arch foot to the vault, resulting in an increase in point cloud error with increasing scanning distance towards the vault. Increasing the number of scanning sites is necessary to obtain higher precision data points capable of meeting the accuracy requirements of bridge construction control.

3.3 Analysis of Main Arch Line Shape in Conjunction with Building Information Modelling

Three-dimensional laser scanning technology can be used to achieve real-time measurements in the construction process and thereby obtain the line shape of the main arch at each construction stage, which can then be contrasted with the corresponding model obtained using building information modelling (BIM) to display changes in the line shape. Simultaneously, the 3D laser scanning technology can be employed with BIM linkage control for making timely adjustments in the control parameters, making the measurement range from point to 3D space surface, and achieving real-time analysis of measurement results. The BIM-based model can be imported into Geomagic Control X software using the Industry Foundation Classes (IFC) model protocol.

This process was analysed using the 1/4 main arch model shown in Fig. 6, in which 1,879,066 triangulations were formed after packaging. This model is acceptable for use because the bridge is a double-symmetrical design. Here, the BIM-based model is used as a reference in the line-shape analysis of the bridge. The point cloud data obtained by 3D laser scanning reflect the main arch line shape in its current construction stage, which, in this study, corresponds with the period after the deck paving was completed. Therefore, the point cloud data are used

Table 6
Coordinate Measurement Results Obtained for Control Points Ranging from the Arch Foot (Point 1) to the Vault (Point 12) based on 3D Laser Scanning and the Leica TCRA 1201+ Total Station

Leica Total Station (m)			3D Laser Scanner (m)			Difference ΔL (mm)		
X	Y	Z	X	Y	Z	X	Y	Z
984,067.68	99,941.87	1,063.00	984,067.68	99,941.87	1,063.00	2.3	3.1	2.0
984,061.73	99,933.78	1,069.42	984,061.73	99,933.78	1,069.41	1.6	2.8	3.1
984,055.80	99,925.76	1,075.21	984,055.79	99,925.76	1,075.21	2.5	1.9	1.9
984,049.85	99,917.71	1,080.47	984,049.84	99,917.70	1,080.46	3.0	2.4	3.8
984,043.89	99,909.65	1,085.19	984,043.88	99,909.64	1,085.19	3.4	3.0	3.1
984,029.92	99,907.52	1,089.41	984,029.91	99,907.51	1,089.41	3.7	4.7	4.3
984,010.04	99,909.20	1,093.30	984,010.04	99,909.19	1,093.30	3.9	5.2	5.0
984,026.06	99,885.46	1,096.37	984,026.06	99,885.46	1,096.37	4.6	6.5	5.7
984,020.12	99,877.41	1,099.18	984,020.11	99,877.40	1,099.17	5.0	7.3	7.9
984,011.18	99,865.33	1,102.52	984,011.17	99,865.32	1,102.51	8.4	8.3	8.0
984,002.28	99,853.26	1,104.86	984,002.28	99,853.25	1,104.85	9.5	9.1	8.6
983,993.38	99,841.12	1,106.22	983,993.37	99,841.11	1,106.21	9.8	9.8	9.5

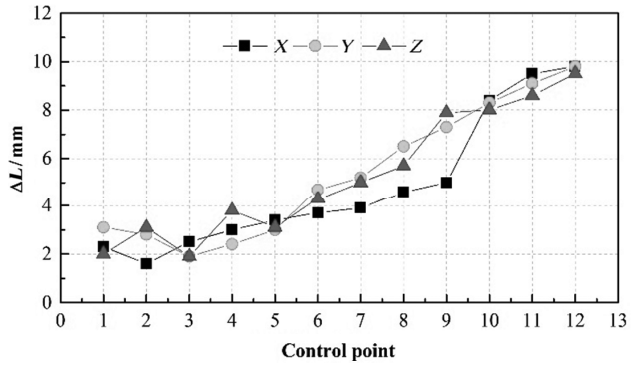

Figure 5. Differences ΔL between the coordinate measurement results obtained in three dimensions from 3D laser scanning and the Leica TCRA 1201+ total station with respect to control points ranging from the arch foot (point 1) to the vault (point 12).

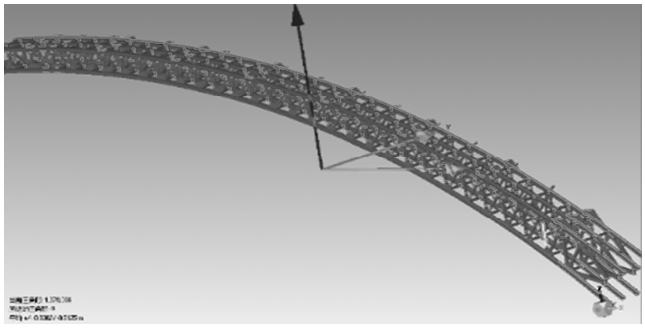

Figure 6. Point cloud diagram of the model obtained by BIM.

as a test. The main arch line shape is then analysed using the 3D comparison module in Geomagic Control X software. Accordingly, comparing the point cloud data with the BIM-based model reflects the 3D line shape of the main arch under the constant load of the bridge and the remaining pre-arch degree of the main arch under the current state. The comparison included the coordinates of 14 measurement points obtained at equal intervals along the 1/4 span of the main arch, as illustrated in Fig. 6. The results in the local coordinate system are listed in Table 7. Here, the BIM-based model coordinates are given in three dimensions as Rx, Ry, and Rz, while the corresponding coordinates obtained by laser scanning are given as x, y, and z, and the deviations between the two results in the x, y, and z directions are respectively given as Dx, Dy, and Dz, where $D = \sqrt{(Dx^2 + Dy^2 + Dz^2)}$.

The deviation results in Table 7 are visually depicted in Fig. 7. As was observed in Fig. 5, the deviation values all increase from the arch footing towards the vault, with the exception of Dx, which initially increases and then decreases. Figure 8 presents a comparison between D and Dz, where Dz represents the pre-camber change of the main arch design. It can be seen that the D values are always greater than Dz by a maximum difference of about 1.5 cm, but the trends in these deviations from arch footing to vault are essentially equivalent. This indicates that 3D laser scanning in conjunction with the BIM-based model can verify the residual pre-camber during the construction of the main arch.

In addition, the reference point and test point coordinates of the main arch employed in 3D visual line analysis are based on the control point as the centre, and the point

Table 7
Comparison of BIM-based Model Coordinates (m) in Three Dimensions (Rx, Ry, and Rz) with Those Obtained by 3D Laser Scanning (x, y, and z) of the Main Arch, Where Dx, Dy, and Dz (cm) are the Deviations between the Two Results in Each Dimension, While D (cm) is the Total Deviation (*i.e.*, $D = \sqrt{(Dx^2 + Dy^2 + Dz^2)}$). Here, R (m) is the Fitting Radius

Points	Rx	Ry	Rz	R	x	y	Z	D	Dx	Dy	Dz
A001	67.064	−5.290	−22.258	0.05	67.066	−5.293	−22.255	0.5	0.3	−0.3	0.3
A002	62.302	−5.299	−18.740	0.05	62.304	−5.299	−18.738	0.2	0.1	−0.1	0.2
A003	57.285	−5.289	−15.207	0.05	57.298	−5.301	−15.188	2.6	1.3	−1.2	1.9
A004	52.285	−5.291	−11.842	0.05	52.2984	−5.304	−11.822	2.7	1.4	−1.3	2.0
A005	47.252	−5.286	−8.631	0.05	47.276	−5.309	−8.593	5.1	2.4	−2.4	3.8
A006	42.271	−5.296	−5.604	0.05	42.295	−5.323	−5.565	5.4	2.4	−2.7	4.0
A007	37.251	−5.285	−2.712	0.05	37.285	−5.319	−2.652	7.7	3.4	−3.5	6.0
A008	32.204	−5.294	0.044	0.05	32.235	−5.331	0.099	7.4	3.1	−3.8	5.5
A009	27.213	−5.294	2.613	0.05	27.246	−5.333	2.681	8.5	3.4	−3.9	6.8
A010	22.147	−5.314	5.075	0.05	22.177	−5.355	5.139	8.2	3.0	−4.1	6.4
A011	17.189	−5.375	7.293	0.05	17.216	−5.426	7.354	8.4	2.7	−5.1	6.1
A012	12.245	−5.305	9.484	0.05	12.272	−5.346	9.549	8.2	2.7	−4.1	6.6
A013	7.166	−5.313	11.519	0.05	7.193	−5.354	11.591	8.7	2.8	−4.1	7.2
A014	2.105	−5.308	13.430	0.05	2.129	−5.353	13.498	8.5	2.3	−4.5	6.8

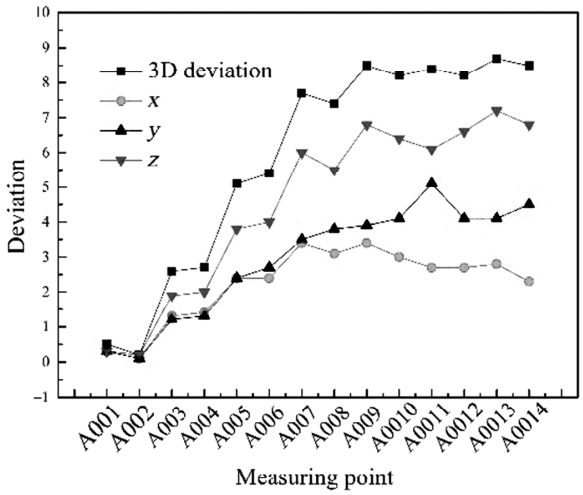

Figure 7. Coordinate Deviations for Each Measurement Point.

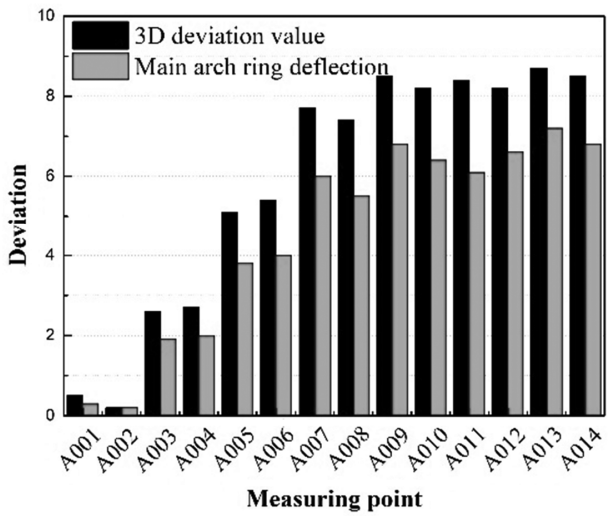

Figure 8. Comparison of Deflection Changes.

cloud within the deviation radius is fitted by the least square method. This reduces the error relative to that obtained by single point measurements in conventional 2D coordinate control, which considers only single point error in the linear analysis because of the limited position of the measurements and the limited number of control points, and therefore achieves poor linear lateral contrast. However, 3D visual line comparison can select the points measured at different positions for 2D analysis, which decreases the linear control error of the main arch.

3.4 Analysis of Temperature Effects on Main Arch

Changes in the alignment of the main arch occurring during the construction of long-span CFST arch bridges directly affect the line shape of the bridge deck, which can decrease its bearing capacity. Variations in the ambient temperature not only affect the preloading of hoisting segments but also have a significant influence on the control of bridge line shape after completion. Therefore, 3D visual line shape analysis is applied to the main arch under an irregular temperature distribution, and the results are compared with the corresponding theoretical and simulation results.

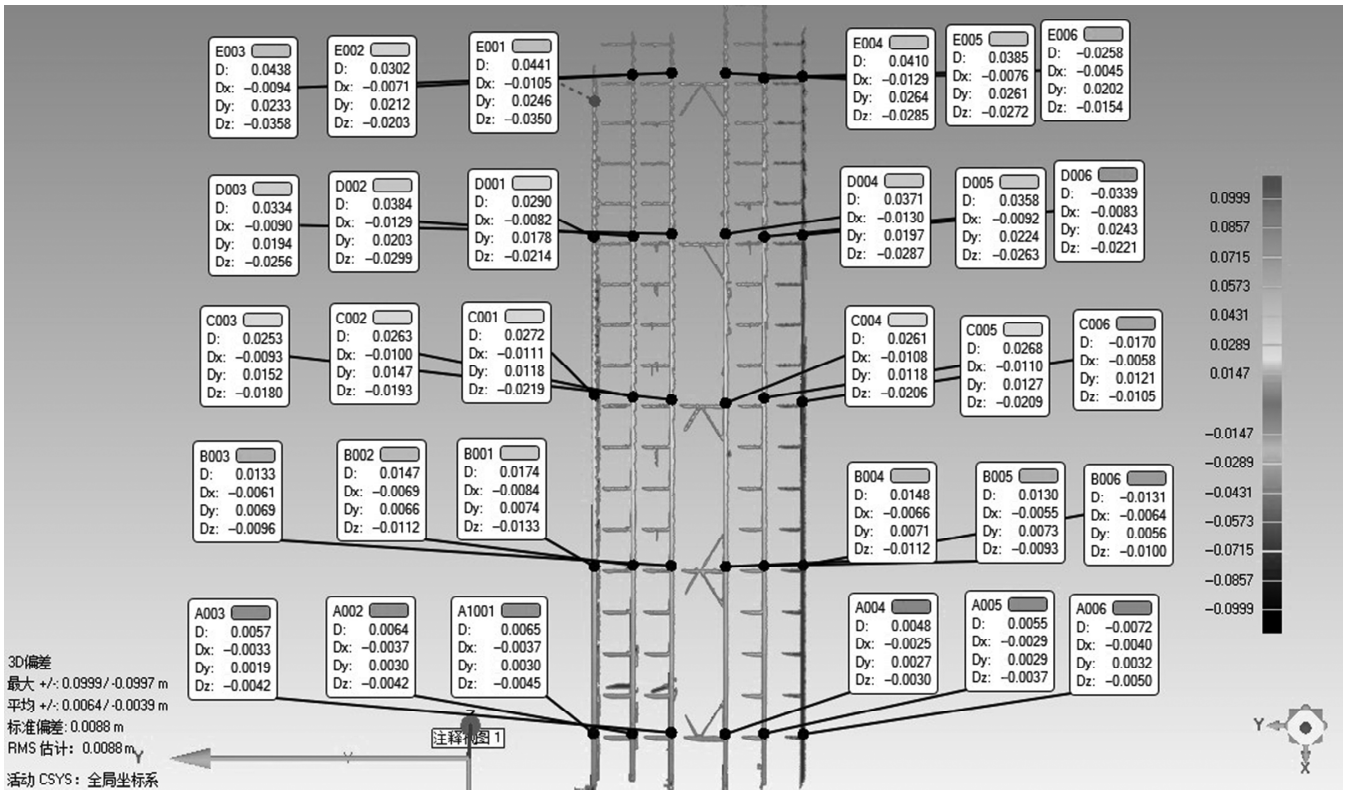

Figure 9. 3D visual line analysis of the linear temperature effect on the main arch at 12:00.

Table 8
Effect of Temperature on the Main Arch Shape (cm)

	Chord 1	Chord 2	Chord 3	Chord 4	Chord 5	Chord 6
Section A	0.65	0.64	0.57	0.48	0.55	−0.72
Section B	1.74	1.47	1.33	1.48	1.3	−1.31
Section C	2.72	2.63	2.53	2.61	2.68	−1.7
Section D	2.9	3.84	3.34	3.71	3.58	−3.39
Section E	4.41	3.02	4.38	4.1	3.85	−2.58

3.4.1 3D Visual Line Analysis of Temperature Effects on the Main Arch

The first group of field data was packaged and processed as a reference. The other three sets of data were used as tests to perform 3D visual line analysis according to the process presented in Section 3.3, and the deviations Dx, Dy, Dz, and D in sections A-E of different chords 1–6 of the main arch are investigated under the irregular temperature loading conditions observed at 12:00, where chord 1 is subjected to direct sunlight, while chord 6 is shaded. The results are shown in Fig. 9, where the magnitudes of the deviations are assigned according to the scale given on the right side of the figure.

As chord 6 is not exposed to direct sunlight in the morning, its surface temperature is significantly less than the surface temperature of chord 1. This is indicated in the figure by the deviations in the different sections of chord 6, which demonstrate that chord 6 is bent downwards (*i.e.*, $D<0$), while the other chords are bent upwards (*i.e.*, $D>0$). In addition, the deviations are observed to increase in magnitude from the arch foot (section A) to the vault (section E), which is caused by long-distance measurement error. These results are clarified by listing the value for each section of each chord in Table 8, which are then plotted in Fig. 10 to enable a convenient visual comparison.

The unique deformation behaviour of chord 6 with respect to temperature was separately analysed at 8:00, 10:00, and 12:00 to evaluate the effect of surface temperature variations on the main arch line shape. Here, the temperature of the shaded side of the bridge increases from 8:00 to 12:00, and the temperature difference between the sunny and shaded sides decreases gradually, such that the surface temperatures of the main arch components become increasingly uniform. Deviations in the line shapes of sections A–E of chord 6 are plotted in Fig. 11(a) with respect to time. It can be seen from the figure that the transverse

Table 9
Changes in the Line Shape (cm) for Control Sections A–E of Chords 1–6 of the Main Arch Under the Two Temperature Loading Schemes

	Scheme 1					Scheme 2				
Section/Chord	A	B	C	D	E	A	B	C	D	E
Chord 1	0.08	0.76	1.63	2.61	3.59	0.02	0.30	0.71	1.16	1.61
Chord 2	0.07	0.63	1.33	2.11	2.89	0.04	0.27	0.56	0.88	1.21
Chord 3	0.04	0.45	0.99	1.57	2.15	0.02	0.14	0.32	0.54	0.76
Chord 4	0.03	0.21	0.48	0.80	1.12	0.01	0.05	0.11	0.19	0.26
Chord 5	0.01	0.06	0.16	0.29	0.42	0.00	−0.02	−0.05	−0.07	−0.10
Chord 6	0.00	−0.08	−0.15	−0.21	−0.26	0.00	−0.08	−0.20	−0.33	−0.46

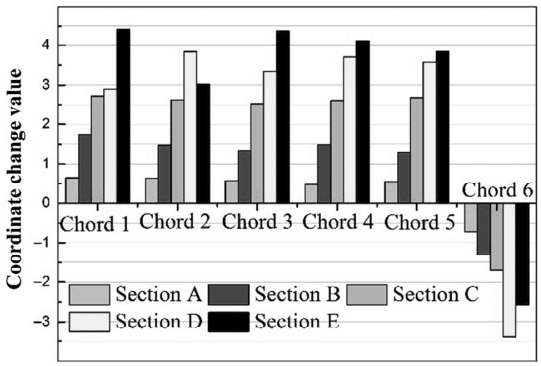

Figure 10. Plotting of the results in Table 8 for enabling convenient visual comparison.

temperature difference of the main arch decreases from 8:00 to 12:00, and the direction of deformation of each section of chord 6 reverses at 10:00. These results are clarified by plotting the absolute values of the line deviations of sections A–E at 8:00, 10:00, and 12:00 in Fig. 11(b), which shows that the deformation value of the reduced chord 6 keeps decreasing, that is, the chord 6 line rises relatively.

3.4.2 Theoretical and Simulation Analyses of Temperature Effects on the Main Arch

When the main arch structure is completed, the arch feet are fixed on both sides. As such, the main arch is a three-time statically indeterminate structure during the process of bridge construction. The deformation in the main arch due to a temperature change Δt is restricted by redundant constraints, which generates internal forces [14]. This condition is illustrated in Fig. 12.

An analysis of Fig. 12 yields the following expression of main arch deformation Δ_K due to a temperature change Δt:

$$\Delta_K = \Delta_{KN} + \Delta_{Kt}, \tag{12}$$

where Δ_{KN} is the deformation caused the internal force generated by the excess constraint and Δ_{Kt} is the deformation caused by Δt. These terms are individually defined as follows:

$$\Delta_{KN} = \sum \int \frac{\overline{M}_k M_{ds}}{EI} \tag{13}$$

$$\Delta_{KN} = \sum \overline{F}_{NK} \alpha t S - \sum \frac{\alpha \Delta t}{h} \int \overline{M}_k ds \tag{14}$$

$$M = \overline{M}_{\overline{F}_{NK}} F_{NK} + \overline{M}_{\overline{F}_{SK}} F_{SK} + \overline{M}_{\overline{M}_K} M_K. \tag{15}$$

Here, MK is the basic system displacement, and FNK and FSK are the internal forces of the main arch caused by the excess constraint, which are illustrated in Fig. 12, EI is the structural bending stiffness, α is the linear expansion coefficient of the main arch material, S is the arc length of the main arch, and h is the height of the main arch.

A 3D finite element model of the main arch segment in the hoisting and arch construction stage was established using Midas/Civil finite element analysis software, and the model is shown in Fig. 13.

According to the linear deformation analysis of the main arch conducted in Section 3.4.1, two temperature loading schemes were adopted with $\Delta t = 10°\mathrm{C}$ applied to only a portion of the main arch. In Scheme 1, the upper and lower chords 1–3 are loaded by Δt, and chords 4–6 are not loaded. In Scheme 2, the upper and lower chords 1 are loaded by Δt, and chords 2–6 are not loaded. Table 9 lists the linear deformation values of the main arch obtained through modelling calculation under the two loading schemes for control sections A–E of chords 1–6, where the minus sign represents the lower deflection. In addition, the results listed in Table 9 for Schemes 1 and 2 are, respectively, plotted in Figs. 14(a) and (b) for easy visual comparison.

As can be seen from Table 9 and Fig. 14, chord 6 undergoes negative displacement even when only chord 1 is subjected to temperature loading, which is consistent with the 3D visual line analysis results presented in Section 3.4.1. In addition, the results presented in Section 3.4.1 demonstrated that the lateral temperature difference of the

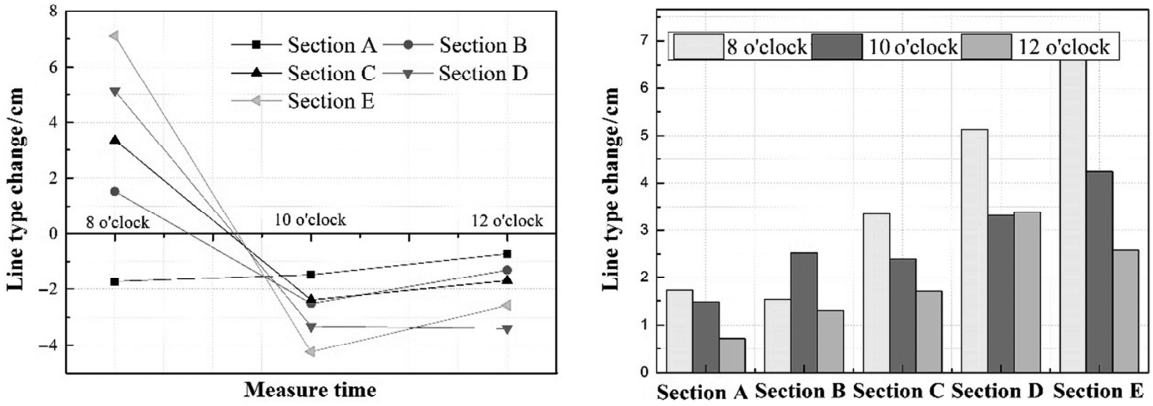

Figure 11. Changes in the line shape of chord 6 under different temperature conditions: (a) with respect to time and (b) absolute value deviations with respect to section.

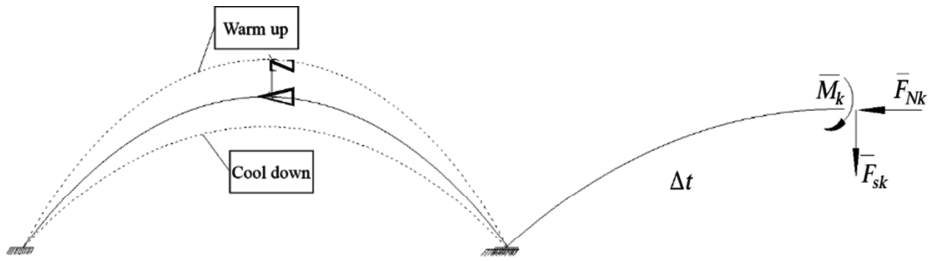

Figure 12. Deformation analysis of the main arch due to a temperature change Δt.

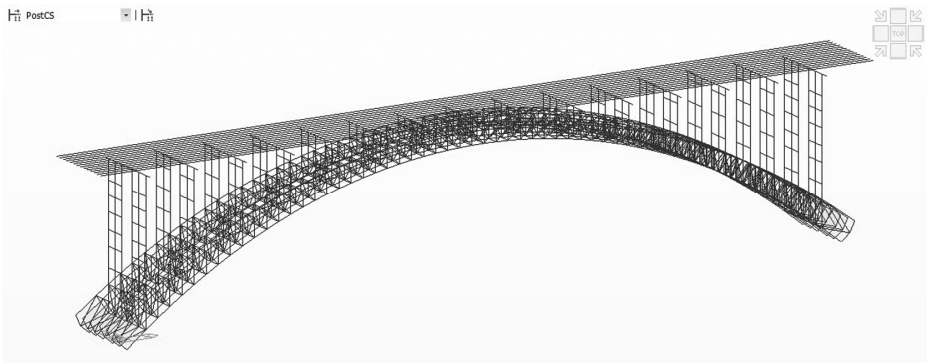

Figure 13. Finite element model of the main arch.

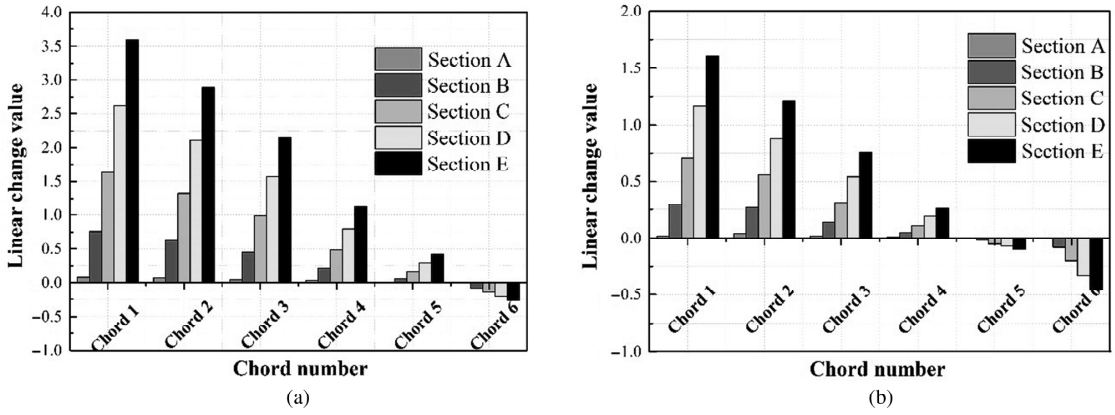

Figure 14. Plotting of the results in Table 9 for enabling convenient visual comparison: (a) Scheme 1 and (b) Scheme 2.

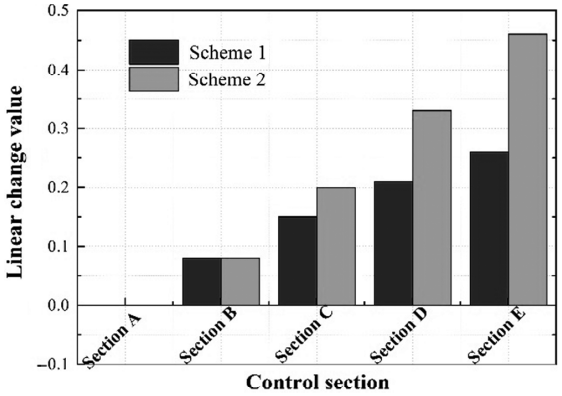

Figure 15. Absolute values of the changes in the line shape (cm) for control sections A–E of chord 6 under the two temperature loading schemes.

main arch decreases with increasing duration of temperature loading, and the respective deformations of the main arch components become increasingly uniform. This was demonstrated in the simulation analysis as well, as shown by the absolute values of the deformations of chord 6 in Fig. 15. As the temperature changes tend to be the same under the two temperature loading schemes, the displacement of each control section of chord 6 gradually decreases, which further verifies the feasibility of 3D visual line shape analysis applied to the main arch under the influence of irregular temperature distributions.

4. Conclusion

This study reported on the application of 3D laser scanning technology for the line type monitoring of a CFST arch bridge with a main span of 300 m under conditions where the temperatures of the main arch components vary due to irregular heating. The study yielded the following conclusions:

(1) The point cloud data obtained from multiple perspectives under 3D laser scanning can be stored and analysed digitally and effectively employed for displaying the bridge line shape during construction in three dimensions. However, multi-view omnidirectional scanning is required to ensure high-precision data.

(2) The measured data were used to reconstruct a 3D model of the main bridge arch, and the error between the obtained model and 98% of the point cloud data was within the accuracy requirement. These results indicate that the captured point cloud data of the bridge exhibited good accuracy and also demonstrated that the point cloud data obtained by 3D laser scanning can be employed for conducting reverse modelling of long-span bridges

(3) Comparisons between the results of 3D visual line shape analysis and the corresponding BIM-based model in each construction stage verified the reliability of 3D laser scanning technology when applied to large-span CFST arch bridges, achieved linkage control with the BIM-based model, and enabled the adjustment of control parameters in real time. The results also demonstrated that 3D visual line shape analysis can verify the residual pre-camber of the main arch during construction, and the error is smaller.

(4) The application of 3D visual line shape analysis to the main arch under irregular temperature distributions corresponded to the results of finite element simulations, which demonstrated the reliability of 3D visual line shape analysis in the visual construction control of CFST arch bridges and also demonstrated the advantages of the approach in comparison with conventional construction measurements.

Acknowledgement

This work was supported by the Science and Technology Project of the Yunnan Provincial Transportation Department (Grant No. [2018]27) and the Graduate Education Innovation Fund Project (Grant Nos. CYS18214 and 2018S0104).

References

[1] S.F. Masri, A.W. Smyth, A.G. Chassiakos, *et al.*, Application of neural network for detection of changes in nonlinear systems, *Journal of Engineering Mechanics*, *126*(7), 2000, 666–676.

[2] Y. Xu, J. Brownjohn, and D. Kong, A non-contact vision-based system for multipoint displacement monitoring in a cable-stayed footbridge, *Structural Control and Health Monitoring*, *25*(5), 2018, 1–23.

[3] S.B. Sholts, S.K.T.S. Wärmländer, L.M. Flores, K.W.P. Miller, and P.L. Walker, Variation in the measurement of cranial volume and surface area using 3D laser scanning technology, *Journal of Forensic Sciences*, *55*(4), 2010, 871–876.

[4] S. Sandhu and S. Dreckmann, A description of the ligament length of the index and long proximal interphalangeal joints using 3D laser scanning, *International Journal of Surgery*, *11*(8), 2013, 679.

[5] D.L. Ma and J. Cui, Application and research of 3D laser scanning technology in steel structure installation and deformation monitoring, *Applied Mechanics and Materials*, *580–583*, 2014, 2838–2841.

[6] H. Wang and T.Y. Tao, Structural health monitoring system for Sutong Cable-stayed Bridge, *Smart Structures & Systems*, *18*(2), 2016, 317–334.

[7] S. Yoon, Q. Wang, and H. Sohn, Optimal placement of precast bridge deck slabs with respect to precast girders using 3D laser scanning, *Automation in Construction*, *86*, 2018, 81–98.

[8] B. Riveiro, P. Morer, P. Arias, *et al.*, Terrestrial laser scanning and limit analysis of masonry arch bridges, *Construction & Building Materials*, *25*(4) 2011, 1726–1735.

[9] A. Soni, S. Robson, and B. Gleeson, Structural monitoring for the rail industry using conventional survey, laser scanning and photogrammetry, *Applied Geomatics*, *7*(2), 2015, 123–138.

[10] M.G. Chen, C.S. Chen, C.T. Wu, *et al.*, Monitoring of sag deformation in suspension bridges using a 3D Laser Scanner, *Circulation Research*, *115*(5), 2010, 475–486.

[11] L.F. Zhang and H.M. Lu, The research and application of 3D Laser Scanning Measurement Technology in Forestry, *Key Engineering Materials*, *419*, 2010, 301–304.

[12] B. Mederos, Point cloud denoising, *Proceeding of SIAM Conference on Geometric Design and Computing*, Citeseer, CA, 2003, 1–11.

[13] H. Lin, D.Q. Gao, and J.M. Yi, Surface reconstruction and Nc simulation of auto rear view mirror based on Geomagic studio, *Applied & Mechanics & Materials*, *271*, 2012, 515–518.

[14] Y.F. Wang, Y.S. Ma, and B. Han, Temperature effect on creep behavior of CFST arch bridges, *Journal of Bridge Engineering*, *18*(12), 2013, 1397–1405.

Biographies

Mingshu Sun was born in October 1973 and belongs to Han nationality. He is the member of the Communist Party of China. He received his master degree in Management in Qujing, Yunnan. He is the Senior Engineer and the First Class Construction Engineer of highway engineering and construction engineering. Currently, he is the Deputy Secretary and the Chairman of the Party Committee of Southwest Transportation Construction Group Co., Ltd., Sichuan, China.

Anqi Xu was born in 1994. He is now doing his master degree. In 2017, he graduated from the Chongqing Jiaotong University with a bachelor degree in Engineering. His research interests are bridge performance evaluation and reinforcement. He is now working in CCCC Second Harbour Engineering Co., Ltd. National Enterprise Technology Center.

Jian Liu was born in 1993. He is now doing his master degree. In 2015, he graduated from the Chongqing Jiaotong University with a master degree in Engineering. His research interests are bridge performance evaluation and reinforcement. He is now working for CMCU Engineering Co., Ltd.